AGN STORM 2. V. Anomalous Behavior of the C IV Light Curve of Mrk 817[*]

Y. Homayouni[1,2,3], Gerard A. Kriss[1], Gisella De Rosa[1], Rachel Plesha[1], Edward M. Cackett[4], Michael R. Goad[5], Kirk T. Korista[6], Keith Horne[7], Travis Fischer[8], Tim Waters[9], Aaron J. Barth[10], Erin A. Kara[11], Hermine Landt[12], Nahum Arav[13], Benjamin D. Boizelle[14], Misty C. Bentz[15], Michael S. Brotherton[16], Doron Chelouche[17,18], Elena Dalla Bontà[19,20], Maryam Dehghanian[21], Pu Du[22], Gary J. Ferland[21], Carina Fian[18,23], Jonathan Gelbord[24], Catherine J. Grier[25], Patrick B. Hall[26], Chen Hu[22], Dragana Ilić[27,28], Michael D. Joner[14], Jelle Kaastra[29,30], Shai Kaspi[23], Andjelka B. Kovačević[27], Daniel Kynoch[31,32], Yan-Rong Li[22], Missagh Mehdipour[1], Jake A. Miller[4], Jake Mitchell[12], John Montano[10], Hagai Netzer[23], J. M. M. Neustadt[33], Ethan Partington[4], Luka Č. Popović[27,34], Daniel Proga[9], Thaisa Storchi-Bergmann[35], David Sanmartim[36], Matthew R. Siebert[37], Tommaso Treu[38,45], Marianne Vestergaard[39,40], Jian-Min Wang[22,41,42], Martin J. Ward[12], Fatima Zaidouni[11], and Ying Zu[43,44]

[1] Space Telescope Science Institute, 3700 San Martin Drive, Baltimore, MD 21218, USA
[2] Department of Astronomy and Astrophysics, The Pennsylvania State University, 525 Davey Laboratory, University Park, PA 16802, USA
[3] Institute for Gravitation and the Cosmos, The Pennsylvania State University, University Park, PA 16802, USA
[4] Department of Physics and Astronomy, Wayne State University, 666 W. Hancock Street, Detroit, MI 48201, USA
[5] School of Physics and Astronomy, University of Leicester, University Road, Leicester LE1 7RH, UK
[6] Department of Physics, Western Michigan University, 1120 Everett Tower, Kalamazoo, MI 49008-5252, USA
[7] SUPA School of Physics and Astronomy, North Haugh, St. Andrews KY16 9SS, Scotland, UK
[8] AURA for ESA, Space Telescope Science Institute, 3700 San Martin Drive, Baltimore, MD 21218, USA
[9] Department of Physics & Astronomy, University of Nevada, Las Vegas, 4505 S. Maryland Parkway, Las Vegas, NV 89154-4002, USA
[10] Department of Physics and Astronomy, 4129 Frederick Reines Hall, University of California, Irvine, CA 92697-4575, USA
[11] MIT Kavli Institute for Astrophysics and Space Research, Massachusetts Institute of Technology, Cambridge, MA 02139, USA
[12] Centre for Extragalactic Astronomy, Department of Physics, Durham University, South Road, Durham DH1 3LE, UK
[13] Department of Physics, Virginia Tech, Blacksburg, VA 24061, USA
[14] Department of Physics and Astronomy, N284 ESC, Brigham Young University, Provo, UT 84602, USA
[15] Department of Physics and Astronomy, Georgia State University, 25 Park Place, Suite 605, Atlanta, GA 30303, USA
[16] Department of Physics and Astronomy, University of Wyoming, Laramie, WY 82071, USA
[17] Department of Physics, Faculty of Natural Sciences, University of Haifa, Haifa 3498838, Israel
[18] Haifa Research Center for Theoretical Physics and Astrophysics, University of Haifa, Haifa 3498838, Israel
[19] Dipartimento di Fisica e Astronomia "G. Galilei," Università di Padova, Vicolo dell'Osservatorio 3, I-35122 Padova, Italy
[20] INAF-Osservatorio Astronomico di Padova, Vicolo dell'Osservatorio 5, I-35122 Padova, Italy
[21] Department of Physics and Astronomy, The University of Kentucky, Lexington, KY 40506, USA
[22] Key Laboratory for Particle Astrophysics, Institute of High Energy Physics, Chinese Academy of Sciences, 19B Yuquan Road, Beijing 100049, People's Republic of China
[23] School of Physics and Astronomy and Wise observatory, Tel Aviv University, Tel Aviv 6997801, Israel
[24] Spectral Sciences Inc., 4 Fourth Avenue, Burlington, MA 01803, USA
[25] Department of Astronomy, University of Wisconsin-Madison, Madison, WI 53706, USA
[26] Department of Physics and Astronomy, York University, Toronto, ON M3J 1P3, Canada
[27] University of Belgrade—Faculty of Mathematics, Department of Astronomy, Studentski trg 16, Belgrade, Serbia
[28] Hamburger Sternwarte, Universität Hamburg, Gojenbergsweg 112, D-21029 Hamburg, Germany
[29] SRON Netherlands Institute for Space Research, Niels Bohrweg 4, 2333 CA Leiden, The Netherlands
[30] Leiden Observatory, Leiden University, P.O. Box 9513, 2300 RA Leiden, The Netherlands
[31] School of Physics and Astronomy, University of Southampton, Highfield, Southampton SO17 1BJ, UK
[32] Astronomical Institute of the Czech Academy of Sciences, Boční II 1401, 141 00 Prague, Czechia
[33] Department of Astronomy, The Ohio State University, 140 West 18th Avenue, Columbus, OH 43210, USA
[34] Astronomical Observatory, Volgina 7, 11060 Belgrade, Serbia
[35] Departamento de Astronomia—IF, Universidade Federal do Rio Grande do Sul, CP 150501, 91501-970 Porto Alegre, RS, Brazil
[36] Rubin Observatory Project Office, 950 N. Cherry Avenue, Tucson, AZ 85719, USA
[37] Department of Astronomy and Astrophysics, University of California, Santa Cruz, CA 92064, USA
[38] Department of Physics and Astronomy, University of California, Los Angeles, CA 90095, USA
[39] Steward Observatory, University of Arizona, 933 North Cherry Avenue, Tucson, AZ 85721, USA
[40] DARK, The Niels Bohr Institute, University of Copenhagen, Jagtvej 155, DK-2200 Copenhagen, Denmark
[41] School of Astronomy and Space Sciences, University of Chinese Academy of Sciences, 19A Yuquan Road, Beijing 100049, People's Republic of China
[42] National Astronomical Observatories of China, 20A Datun Road, Beijing 100020, People's Republic of China
[43] Department of Astronomy, School of Physics and Astronomy, Shanghai Jiao Tong University, 800 Dongchuan Road, Shanghai 200240, People's Republic of China
[44] Shanghai Key Laboratory for Particle Physics and Cosmology, Shanghai Jiao Tong University, Shanghai 200240, People's Republic of China

[*] Based on observations made with the NASA/ESA Hubble Space Telescope, obtained at the Space Telescope Science Institute, which is operated by the Association of Universities for Research in Astronomy, Inc., under NASA contract NAS5-26555. These observations are associated with program GO-16196.
[45] Packard Fellow.

1

Abstract

An intensive reverberation mapping campaign of the Seyfert 1 galaxy Mrk 817 using the Cosmic Origins Spectrograph on the Hubble Space Telescope revealed significant variations in the response of broad UV emission lines to fluctuations in the continuum emission. The response of the prominent UV emission lines changes over an $\sim$60 day duration, resulting in distinctly different time lags in the various segments of the light curve over the 14 month observing campaign. One-dimensional echo-mapping models fit these variations if a slowly varying background is included for each emission line. These variations are more evident in the C IV light curve, which is the line least affected by intrinsic absorption in Mrk 817 and least blended with neighboring emission lines. We identify five temporal windows with a distinct emission-line response, and measure their corresponding time delays, which range from 2 to 13 days. These temporal windows are plausibly linked to changes in the UV and X-ray obscuration occurring during these same intervals. The shortest time lags occur during periods with diminishing obscuration, whereas the longest lags occur during periods with rising obscuration. We propose that the obscuring outflow shields the broad UV lines from the ionizing continuum. The resulting change in the spectral energy distribution of the ionizing continuum, as seen by clouds at a range of distances from the nucleus, is responsible for the changes in the line response.

Unified Astronomy Thesaurus concepts: Active galaxies (17); Active galactic nuclei (16); Seyfert galaxies (1447); Galaxy nuclei (609)

1. Introduction

The broad emission-line regions (BLRs) are of paramount importance to the study of active galaxy nuclei (AGN) as they provide a probe of the central regions of AGN and their physical conditions. It has long been established that photoionization by the nuclear continuum is responsible for driving the observed UV emission lines (Krolik 1999). Models predict that photoionization heats the broad-line gas, and that much of the C IV emission is due to collisional excitation processes. The observed far-ultraviolet continuum, i.e., the closest wavelength window to the ionizing continuum, is only a proxy for the ionizing continuum ($\lambda \leqslant 912$ Å) that is generally unobservable due to the Lyman limit of our own Galaxy and the presence of hydrogen in the AGN host galaxy. Changes in the ionizing continuum flux from the central source lead to correlated changes in the broad emission lines produced in the BLR. Nonlinear responses in the broad emission-line fluxes can be caused by a mixture of BLR clouds with a range of column densities and ionization parameters. Additionally, temporal changes in the ionizing flux with a fixed spectral shape will result in nonlinear changes in the emission-line flux for most emission lines (Goad et al. 2004; Goad & Korista 2015). Intrinsic to each object, this nonlinear correlation is nominally referred to as the "intrinsic Baldwin effect" (Kinney et al. 1990; Krolik et al. 1991; Pogge & Peterson 1992; Goad et al. 2004). The complex relationship between the continuum flux, $F_{\text{continuum}}$, and the emission-line flux, F_{line}, can be parameterized by two factors: the reprocessing efficiency and the marginal response. The reprocessing efficiency for some particular emission line is the fraction of incident ionizing photons reprocessed into that emission line, and is related to the equivalent width (EW) of the emission line. Here, the EW is determined relative to our proxy for the time-variable strength of the incident ionizing continuum flux, the flux at 1180 Å. The marginal response of an emission line is a measure of how the reprocessing efficiency changes as a function of the strength of the driving ionizing continuum. This relation is parameterized by $F_{\text{line}} \propto F_{\text{continuum}}^{\eta_{\text{eff}}}$, where η_{eff} is a measure of the instantaneous emission-line response to variations in the ionizing continuum and is typically measured after first removing nonvariable background contamination (e.g., narrow emission lines and host galaxy contribution), and after correcting for

the mean delay between the continuum and emission-line variations. Here, again, we use the strength of the continuum at 1180 Å as a proxy for the strength of the largely unobserved ionizing continuum. The marginal response of an emission line is generally calculated as the logarithmic slope of the F_{line} versus $F_{\text{continuum}}$ relation. In terms of EW, this relationship can be expressed as $\text{EW}_{\text{line}} \propto F_{\text{continuum}}^{\beta}$, with $\beta = \eta_{\text{eff}} - 1$. Generally, emission-line response to continuum variations is weaker than linear, so that $\eta_{\text{eff}} < 1$ (i.e., $\beta < 0$; Pogge & Peterson 1992; Gilbert & Peterson 2003; Goad et al. 2004; Goad & Korista 2014; Goad et al. 2016). This relationship can also explain some of the scatter in the global Baldwin effect, where observations of different AGN exhibit an anticorrelation between emission-line EW and the continuum level (Baldwin 1977; Kinney et al. 1990; Osmer et al. 1994; Cackett & Horne 2006). In this work, we refer to the slope in the F_{line} versus $F_{\text{continuum}}$ relation as the marginal response, while normalization is connected to the line's EW, which characterizes the reprocessing efficiency.

Over the past three decades, reverberation mapping (RM; Blandford & McKee 1982; Peterson 1993; Peterson et al. 2004) has been a successful technique for mapping the inner structure of AGN. The RM technique relies on the following assumptions: (a) the central ionizing source is point-like, (b) the AGN variability at two different wavelengths is causally connected, and (c) the light travel time is the most important timescale. With AGN continua showing variability on timescales of days to years, the time delay between fluctuations in the continuum and the emission-line response is believed to be a measure of the mean physical distance between the continuum-emitting region around the supermassive black hole (SMBH) and the BLR, assuming that the photons travel freely. Assuming that the BLR gas motion is primarily gravitational and dominates the velocity dispersion of the BLR gas, the virial product then provides a means of measuring the SMBH mass and studying the structure of the BLR (Clavel et al. 1991; Horne et al. 1991; Peterson et al. 1991; Kaspi et al. 2000; Peterson et al. 2004; Bentz et al. 2009, 2021; Grier et al. 2013; Pancoast et al. 2014; Barth et al. 2015; Du et al. 2016, 2018; Pei et al. 2017; De Rosa et al. 2018; Brotherton et al. 2020; Bao et al. 2022; U et al. 2022). An extensive review of RM applied at a range of wavelengths has recently been published by Cackett et al. (2021).

To probe the spatial and kinematic structure of the BLR gas, a 1D description of the BLR response function is not sufficient (Welsh & Horne 1991). A more complete form of RM is "velocity-resolved" RM (Bahcall et al. 1972; Blandford & McKee 1982), which measures the projection of the BLR into two observables, the line-of-sight velocity and the time-delay response of the BLR. The 2D velocity-delay map encodes information about the BLR geometry and kinematics (Krolik et al. 1991; Ulrich & Horne 1996; Bentz et al. 2010, 2021; Barth et al. 2011; Pancoast et al. 2011; Grier et al. 2013; Pancoast et al. 2014; Du et al. 2016; Pei et al. 2017; Li et al. 2018; Horne et al. 2021; U et al. 2022; Villafaña et al. 2022). Despite decades of RM observation and several optical velocity-resolved RM campaigns, only one velocity-resolved RM campaign in the UV with the Hubble Space Telescope (HST) has been conducted (De Rosa et al. 2015), and the only other UV velocity-resolved campaign of NGC 4151 was based on IUE monitoring (Ulrich & Horne 1996). This is due to the demanding nature of velocity-resolved RM in terms of data quality, time resolution, and duration (Horne et al. 2004). The Space Telescope and Optical Reverberation Mapping (STORM; De Rosa et al. 2015; Kriss et al. 2019) project used daily observations of NGC 5548 over six months made with the Cosmic Origins Spectrograph (COS; Green et al. 2012) on the HST to carry out velocity-resolved RM. The AGN STORM program (hereafter referred to as AGN STORM 1) was accompanied by near-ultraviolet and X-ray monitoring with the Neil Gehrels Swift Observatory (Edelson et al. 2015; Fausnaugh et al. 2016), optical ground-based spectroscopy (Pei et al. 2017), and four X-ray observations with Chandra (Mathur et al. 2017). AGN STORM 2 is a second such program targeting the Seyfert 1 galaxy Mrk 817 ($z = 0.03146$, $\lambda L_{\lambda 5100} = 43.78$ erg s^{-1}, $M_{BH} = 3.86^{+0.61}_{-0.59} \times 10^7 M_\odot$; Peterson et al. 1998, 2004; Denney et al. 2010; Bentz et al. 2013) with intensive multiwavelength monitoring (see Section 2 for more details).

The AGN STORM 1 observations have unveiled a wealth of information about the structure of the BLR, the accretion disk, and the associated outflowing winds. One of the most unexpected results of the AGN STORM 1 program was that approximately midway into the campaign, the emission lines decorrelated from the continuum fluctuations as manifested in a sudden and sustained drop in the emission-line flux and EW and an apparent lack of response to the continuum flux variations during that period. The lines remained decorrelated for 65–70 days, but became well correlated again at the end of the campaign (Goad et al. 2016). During this anomalous period, the emission-line response amplitude is also significantly lower compared to the observed continuum variations. Similar changes occurred in the high-ionization narrow absorption lines. Both effects may be induced by the presence of outflows that obscure the ionizing flux, resulting in "BLR holidays" (Dehghanian et al. 2019), where the emission lines become weaker and their variations less correlated with those in the continuum (Goad et al. 2016). This implies that the simple RM picture, which relies on continuum/emission-line reverberation, is far more complex than we originally anticipated.

The primary goal of the AGN STORM 2 program is to study a second AGN with intensive multiwavelength monitoring. Although Mrk 817 was selected from spectra taken in 2009 to avoid the X-ray and UV obscuration that complicated the STORM 1 campaign, the first COS spectrum of Mrk 817

showed the presence of strong, broad, blueshifted UV absorption troughs similar to the obscuring outflows seen in many other Seyfert galaxies (Mrk 335: Longinotti et al. 2013, 2019; Parker et al. 2019; NGC 5548: Kaastra et al. 2014; NGC 985: Ebrero et al. 2016; NGC 3783: Mehdipour et al. 2017; and NGC 3227: Wang et al. 2022). Furthermore, X-ray observations of Mrk 817 also showed heavy obscuration (Kara et al. 2021; Miller et al. 2021). Changes in X-ray and UV obscuration occur at the same time, suggesting a common origin (Partington et al. 2023).

As for NGC 5548 in STORM 1, the obscuration in Mrk 817 seems to have a significant influence on the response of the BLR. In Kara et al. (2021), hereafter Paper I, analysis of the first 90 days of the STORM 2 campaign showed decorrelation of the emission-line fluxes from the continuum during the first ~55 days. Analysis of the full campaign by Homayouni et al. (2023; hereafter referred to as Paper II) showed that this was not a persistent decorrelation. Instead, it was found to occur in multiple temporal windows throughout the campaign, during which the response of the BLR to continuum fluctuations changed dramatically. Contrary to the basic assumptions underlying RM analysis, the emission-line light curves are not simply a smoothed, scaled, and shifted version of the continuum light curve.

This paper, the fifth in a series describing the AGN STORM 2 results, focuses on the anomalous response of the BLR, particularly for the C IV emission because it is the least contaminated by the obscuring absorption lines, and the least blended with adjacent emission lines. Similar anomalous continuum responses have also been reported by Cackett et al. (2023) in studying Swift light curves. The present work has two primary goals. The first is to identify the different temporal windows where the BLR response to continuum variations significantly changes, and thus affects the measured lag throughout the campaign. The second goal is to understand the role of obscuration in the reprocessing of radiation and its impact on the BLR lag. We briefly describe the HST observations in Section 2. We present the anomalous BLR variations in Section 3. We discuss the implication of our results in Section 4 and summarize our findings in Section 5. We adopt a Lambda cold dark matter (ΛCDM) cosmology with $\Omega_\Lambda = 0.7$, $\Omega_M = 0.3$, and $H_0 = 70$ km s^{-1} Mpc^{-1}. Throughout this work, we refer to observation times as "truncated HJDs" (i.e., THJD = HJD–2,450,000).

2. The STORM 2 Monitoring Campaign of Mrk 817

The AGN STORM 2 program on Mrk 817 consists primarily of 165 epochs of HST observations[46] using COS with the G130M and G160M gratings to cover the 1070–1750 Å range in single-orbit visits with an approximately 2 day cadence. The HST program began on 2020 November 24 and ended on 2022 February 24. Paper II extensively describes the HST program, data products, and COS spectral calibration along with full campaign results. The AGN STORM 2 data products are available at MAST doi:10.17909/N734-K698 (Plesha et al. 2023). During the UV monitoring, the HST program suffered two extended safing incidents resulting in month-long gaps in the HST UV coverage (see Figure 1). Coordinated photometry and spectroscopy supplemented the HST observations, resulting in full X-ray to near-infrared coverage of Mrk 817 over
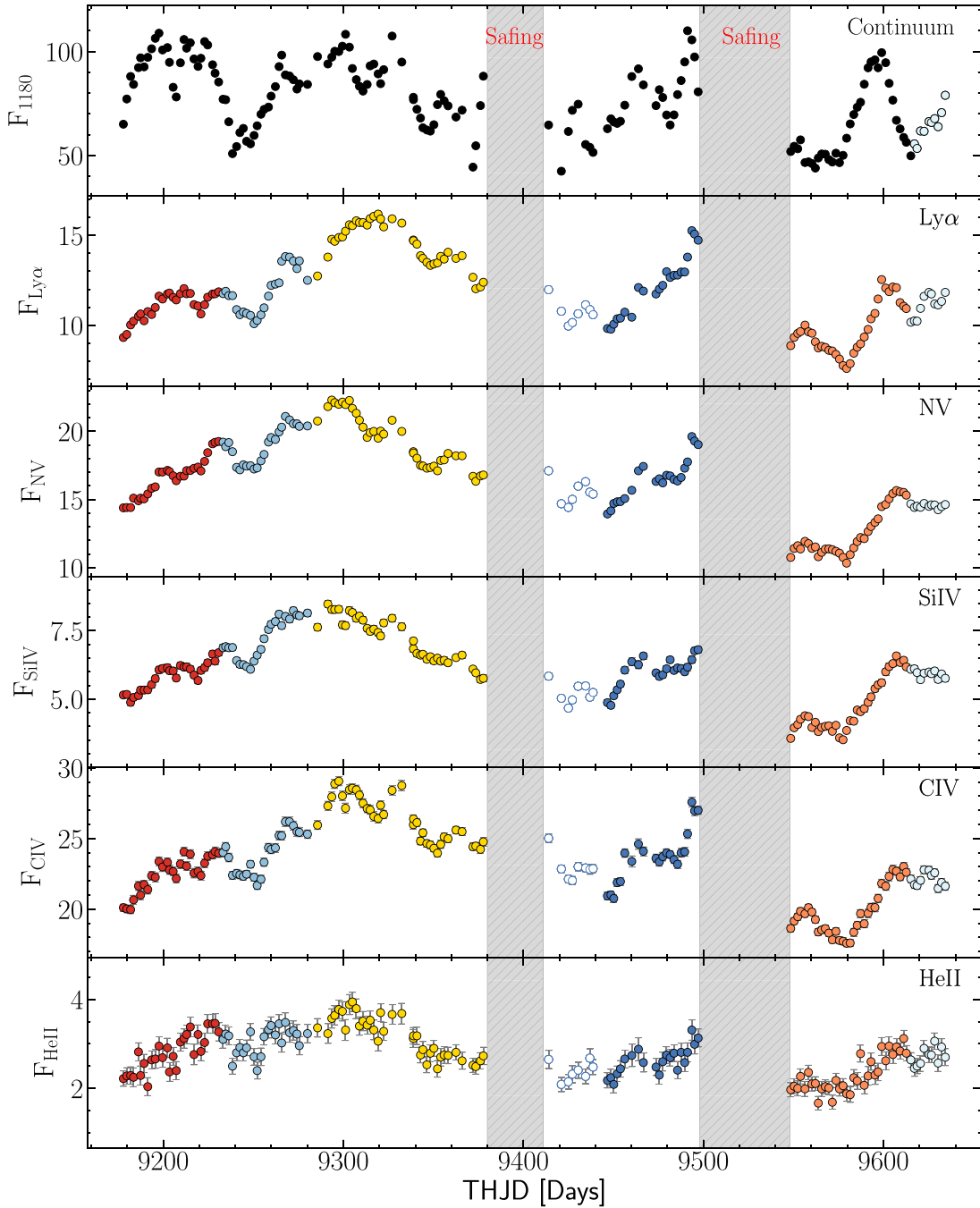
---

[46] HST-GO-16196; Peterson et al. (2020).

Figure 1. Continuum light curve at 1180 Å (top panel) and emission-line light curves for Lyα, N V, Si IV +]O IV, C IV, and He II (bottom panels). All the light curves are presented in the observed frame. The continuum flux is in units of 10^{-15} erg s^{-1} cm^{-2} Å^{-1} and the line fluxes are in units of 10^{-13} erg s^{-1} cm^{-2}. The hashed gray regions display the two major observation gaps due to HST safing incidents. The color schemes for the data points correspond to different light-curve variation regimes that will be discussed throughout this paper. The open blue symbols between THJD = 9410–9440 (in Window 4) are the eight epochs where the HST observations were more sparsely sampled after an extended safing event and are excluded from the rest of the analysis (see the Appendix for details). The Lyα flux is integrated over the blue wing of the emission line to avoid contamination by time-variable absorption features and also N V emission. Similarly, the C IV light curve excludes the blue wing of the line profile because of time-variable absorption (Paper II). The full Lyα and C IV line fluxes are about 5× and 1.6× greater, respectively, than indicated here (see Table 2 of Paper II). Nevertheless, we present these baseline measurements to demonstrate that, while individual emission-line fluxes may not be entirely representative of the total flux, the anomalous characteristics, including those evident in C IV, broadly manifest across all emission lines.

15 months (see Paper I for a campaign overview). Details of those additional observations will be described in a series of follow-up papers.

3. Anomaly in the BLR

The year-long monitoring of Mrk 817 affords a unique opportunity to study the emission-line variations over an extended period. Paper I gives an overview of the STORM 2 campaign and its early results. As shown in Paper I, during the first 90 days of the campaign, the emission-line flux was only weakly correlated with the continuum. Paper II shows that the emission-line light curves are not just smoothed, scaled, and shifted transformations of the continuum light curve. Examining the light curves from the whole campaign (see Figure 1)
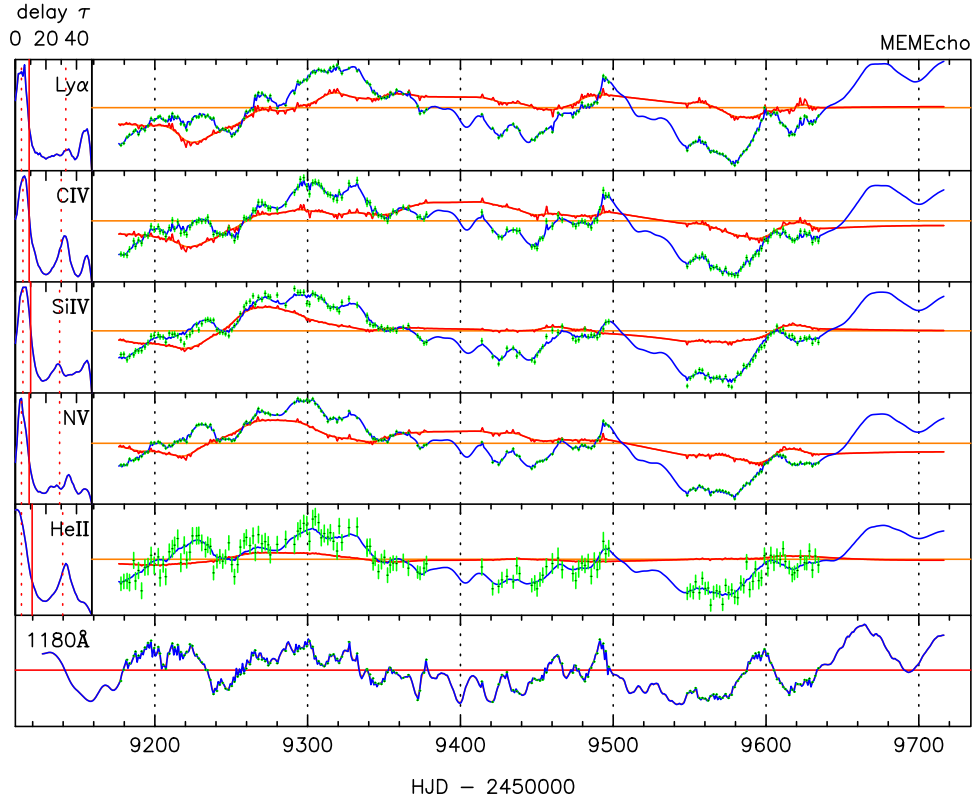
Figure 2. MEMEcho fits to the 1180 Å continuum and five emission-line light curves for Mrk 817 in the STORM 2 campaign. The bottom panel shows the 1180 Å continuum light curve (black points with green error bars), which is the driving light curve. The red horizontal line is the reference level at the median of the data. The top panels show the five emission-line light curves (right) and corresponding delay maps (left). The black points with green error bars show the light-curve data, and the blue curves show the echo models. The red curves show the slow background variations. The vertical red line in each delay map marks the median observed-frame delay, and the vertical dashed red lines mark the quartiles of the delay distributions. The MEMECHO models account for much of the light-curve structure as echoes of the driving light curve, but they also require significant additional variations (red curves).

shows that even though the continuum at the beginning of the campaign is near its peak brightness, the emission lines are low and rising (red points in Figure 1). However, after the emission-line peak at THJD = 9232, the broad line variations became stronger and more representative of the continuum variations. Similar periods of weak correlation reverting to a strong response to continuum fluctuations occur throughout the remaining year of the campaign.

3.1. 1D Linearized Echo Models

Inspired by the anomalous emission-line responses exhibited by NGC 5548 during STORM 1, we set out to analyze the light curves for Mrk 817 in STORM 2 in a model-independent way. We used the maximum entropy method (MEM) implemented in a code called MEMECHO for estimating time delays in AGN RM (Horne et al. 1991; Horne 1994) to obtain a 1D linearized echo model (Horne et al. 2021). Our model uses the 1180 Å continuum light curve, $C(t)$, as the driver, assuming it is a proxy for the ionizing continuum. For a time delay of τ, the flux $L(t)$ of each emission line is a nonlinear function of the continuum light curve shifted to an earlier time, $t - \tau$. MEMECHO linearizes the problem by decomposing the line and continuum light curves into reference levels L_0 and C_0 with variations $\Delta L(t)$ and $\Delta C(t)$ that are tangent-curve approximations to the parent nonlinear functions. With the continuum light curve expressed as

$$C(t) = C_0 + \Delta C(t), \qquad (1)$$

the emission-line light curve is then a convolution of the continuum variations with the 1D delay distribution, $\Psi(\tau)$

$$L(t) = L_0(t) + \int \Psi(\tau) \Delta C(t - \tau) d\tau. \qquad (2)$$

Similar to the analysis of NGC 5548, we allow for a time-dependent background for each of the modeled emission lines, $L_0(t)$. The maximum entropy regularization employed by MEMECHO keeps the resulting delay maps positive and produces solutions that are as smooth as possible.

Figure 2 shows the results of modeling the STORM 2 light curves with the function in Equation (2). The driving light curve, $C(t)$, is the 1180 Å continuum shown in the bottom panel, with the reference level C_0 shown as a red horizontal line. The top five panels show the emission-line light curves with the data points in black, the error bars in green, and the modeled MEMEecho light curves in blue. The left column of the figure shows the derived delay maps for each of the emission lines. The MEMECHO solution produces a static, 1D delay map for each line that is a good fit to the data. However, it does require large variations in the background levels for each emission line, $L_0(t)$, as shown by the red curves in each panel.

Significantly, the large excursions below the mean from the beginning of the campaign to THJD ∼ 9260, and again around THJD = 9600, correspond to temporal windows during the STORM 2 campaign when absorption was the strongest (as we will show later). Similarly, absorption was weakest during the
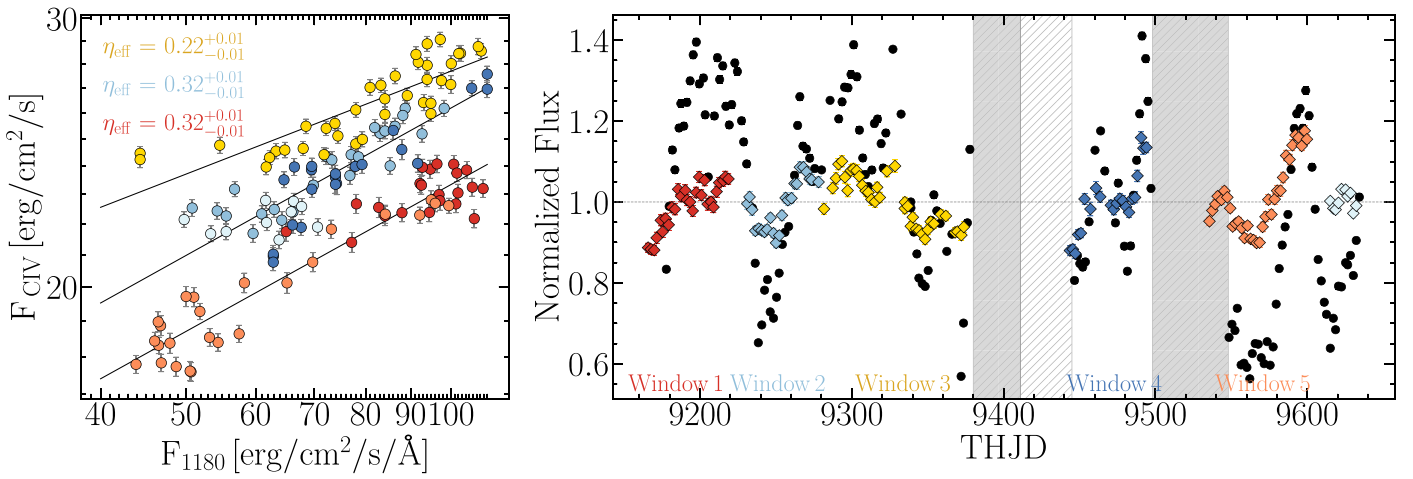
5

Figure 3. Left: the "time-delay-corrected" $F_{C IV}$ (in units of 10^{-13} erg s^{-1} cm^{-2} Å^{-1}) vs. the F_{1180} continuum (in units of 10^{-15} erg s^{-1} cm^{-2} Å^{-1}) measurements displayed on a logarithmic scale. Here the $F_{C IV}$ is "time-delay-corrected" based on the lag measurements in Table 2 (see Section 3.3 for detail). The color coding represents the identified windows in Table 1 using the same color scheme as in Figure 1. We identify three main trends in the C IV emission-line response to continuum variations. The best-fit slope to each trend is illustrated with a black line representing the emission-line response, η_{eff}, for each group of data points. In contrast to the majority of points which show a positive correlation between $F_{C IV}$ and F_{1180}, the observations during the last $\sim$3 weeks of data (light blue points) show no correlated variability, and have a flat response. Right: the C IV light curve (colored symbols) superposed on the continuum light curve (black symbols). The continuum light curve is normalized to its median while the C IV light curve is normalized to the median in each segment, where each segment is shifted based on the lag measurement in each of the identified windows in Table 1. We adopt a zero time delay for the last $\sim$3 weeks of data (light blue data points) as the lag measurement in the final window is consistent with zero lag.

time interval from THJD $\sim$ 9300–9400 when the background levels vary above the mean.

The delay maps of the emission lines have strong peaks with delays $\sim$ 5 days, with He II showing the shortest delay. While the central region is where most of the response is located, there is a secondary peak with a delay $\sim$ 30 days, particularly for C IV and He II.

3.2. Understanding the Anomalous C IV Light Curve

Although the MEMECHO analysis successfully yields static 1D delay maps for the BLR, there is no inherent physical motivation accounting for the slowly varying background required by the model. However, these are real, significant variations the physics of which are not well understood and the MEMECHO approach is only driven by the data behavior. Here we develop a plausible physical explanation for the time-varying background. We start with the anticipated correlation between the flux of the C IV emission line, $F_{C IV}$, and the continuum flux, F_{1180}. We choose F_{1180} as our reference since it is the closest uncontaminated continuum window (by absorption) to the ionizing continuum. As shown in Figure 3, while there is an overall positive correlation between the delay-shifted $F_{C IV}$ and F_{1180}: as the $F_{C IV}$ rises by 25% and F_{1180} doubles (see Section 3.4), there is an 8% rms scatter around the best-fit line to the full campaign. The $F_{C IV}$–F_{1180} correlation seem to show a similar marginal response (see η_{eff} reported in Figure 3) throughout the campaign. However, if we examine this correlation with points selected by observation time (THJD), we see that for several temporal windows, the normalization appears to change between one temporal window to the next. In fact, we can measure an independent and slightly different $F_{C IV} \propto F_{1180}$ response relation for each of these temporal windows, which reduce the rms scatter around each individual best-fit line to $\approx$2%–3%. This may be an indication of a reduction in ionizing photons incident on BLR gas, not tracked by continuum luminosity changes. Table 1 summarizes the start and end times of these temporal windows (details of

Table 1
Emission-line Response Windows

Window	THJD (Days)	Calendar Date (Days)	Duration (Days)
1	9177–9232	2020-11-24 to 2021-01-18	55
2	9232–9282	2021-01-18 to 2021-03-09	50
3	9282–9378	2021-03-09 to 2021-06-13	96
Gap	9378–9413	2021-06-13 to 2021-07-18	36
4[a]	9413–9498	2021-07-18 to 2021-10-11	87
Gap	9498–9548	2021-10-11 to 2021-11-30	51
5	9548–9615	2021-11-30 to 2022-02-05	67
6	9615–9634	2022-02-05 to 2022-02-24	19

Note.
[a] We later redefine Window 4 in Table 2 to include only THJDs from 9445 to 9498. Also, see the discussion in the Appendix.

the selection process for the window boundaries are given in the Appendix). Each window is indicated by a different color in Figure 3, with the corresponding power-law response relations for different families of points overlaid on the plot (see the left panel in Figure 3).

The temporal windows corresponding to these families of points are color coded similarly to the light curves shown in Figure 1. All the UV emission lines except C IV are affected by broad absorption troughs or blended emission-line wings (see Paper I and Paper II), and thus require detailed modeling and deblending (G. A. Kriss et al. 2024, in preparation). Thus, for the remainder of this work, we concentrate on the C IV light-curve behavior. Below, we discuss in more detail the time-delay measurements for C IV as a function of the significant variations with time in its response to the observed continuum.

3.3. Time-varying Lags for C IV

Previous ground-based optical RM campaigns targeting Mrk 817 (Peterson et al. 1998; Denney et al. 2010) successfully

Table 2
C IV Lag Measurements (PyCCF)

Window	THJD (Days)	Time Delay (Days)	r_{max}	N Data Points
1	9177–9232	$11.7^{+0.9}_{-10.3}$	0.66	28
2	9232–9282	$1.9^{+0.5}_{-1.0}$	0.93	24
3	9282–9378	$3.9^{+1.0}_{-1.1}$	0.91	38
4[a]	9445–9498	$2.9^{+0.6}_{-1.4}$	0.90	22
5	9548–9615	$12.5^{+0.6}_{-1.3}$	0.96	34

Note.
[a] Window 4 is shortened to remove the sparse sampling interval ~ 30 days that immediately occurs after the first safing event (see the Appendix for a detailed discussion).

measured Hβ time delays of 14–34 days relative to the 5100 Å continuum. Early campaign results in Paper I suggest that there is an ~ 4 day time delay between the F_{1180} and Swift V band. Paper I Figure 14 shows a Hβ lag of 23.2 ± 1.6 days behind the continuum. The C IV time delay is expected to be half of the observed Hβ lag, motivated by Lira et al. (2018). Paper II finds a time delay of $11.8^{+3.0}_{-2.8}$ days between the F_{1180} and the C IV emission line using the full set of HST UV observations, which is consistent with this prediction. However, as we argued above, this single time-delay measurement does not fully capture the diverse line responses. Therefore, here we study each of the identified windows in Table 2 independently.

We adopt the Python implementation of the commonly used time-series cross-correlation function (CCF) analysis method (PyCCF; Sun et al. 2018) to measure the mean time delay between the F_{1180} continuum and the C IV emission-line flux variations and compute the cross-correlation Pearson correlation coefficient r as a function of time delay τ (often referred to as the interpolated cross-correlation function (ICCF); Gaskell & Sparke 1986; Gaskell & Peterson 1987; White & Peterson 1994) for each of the five temporal windows. We use ± 25 days for the lag search range in each of the temporal windows, though we use ± 50 days for the full campaign results (top panel in Figure 4). We estimate the uncertainty in τ_{ICCF} using Monte Carlo (MC) simulations that employ flux randomization (FR) and random subset sampling (RSS; Peterson et al. 1998). We adopt 20,000 MC iterations to obtain the cross-correlation centroid distributions (CCCDs; Peterson et al. 1998, 2004). To ensure that the time-delay measurements are not due to our choice of lag measurement method, we also use the Z-transformed discrete cross-correlation function (ZDCF) approach (Alexander 1997, 2013; Kovačević & Popović 2017) in combination with Gaussian process (GP) regression to model the stochastic AGN light curves with arbitrary sampling. We find that the ZDCF approach recovers similar time-delay measurements as the PyCCF approach in each of the temporal windows, with time delays consistent within 1σ. We report rest-frame lag measurements in Table 2, along with the cross-correlation coefficients and number of data points in each of the temporal windows. The CCCDs from PyCCF reported in Figure 4 reveal significantly different results for each of the temporal windows. The CCCDs show a clear bimodal distribution across the five temporal windows where two typical time lag results are measured: one at 2–3 days and one at 11–12 days. In particular, the mean time delays corresponding to Windows 1 and 5 (i.e., red and orange, respectively, in Figure 3) are significantly longer than the time
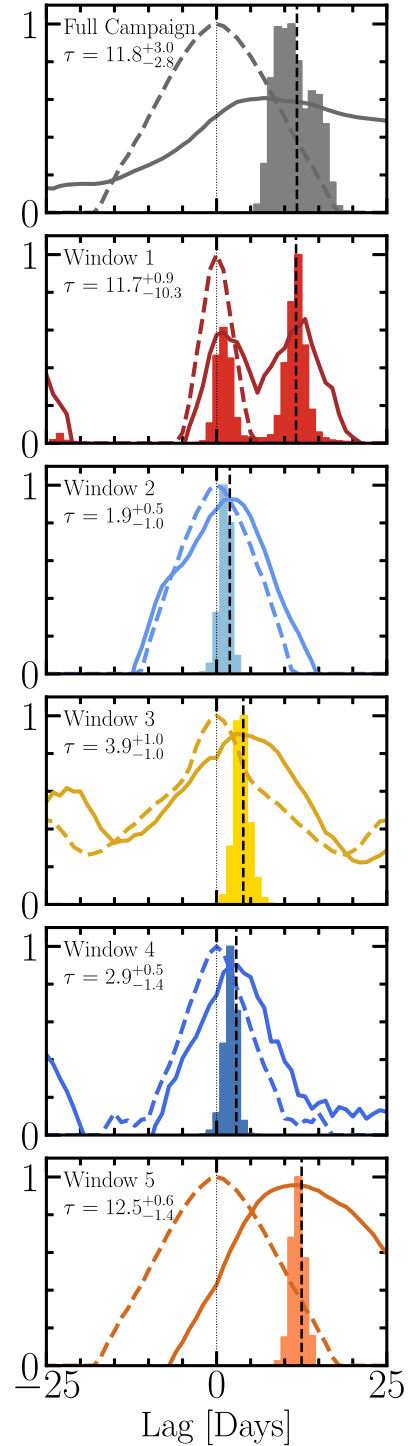

Figure 4. The CCF (solid line) between F_{1180} continuum and C IV in the full campaign (top panel) compared with the CCF computed for each time interval defined in Table 2 (bottom panels). The dashed line shows the autocorrelation function of the continuum in the respective time intervals along with the PyCCF CCCD. The rest-frame lag for each time interval is shown by a vertical dashed line and also reported in Table 2. We find that the C IV CCCD changes significantly over each of the windows, where Windows 1 and 5 prefer a long lag (≈ 12 days), while Windows 2, 3, and 4 have a shorter lag (≈ 2–4 days). Window 1 shows a secondary peak at a shorter time delay that is similar to Windows 2, 3, and 4. However, the longer lag seems to be the dominant peak in Window 1 CCCD.

delay measured for Window 3 (gold), which is slightly longer than the ones obtained for Windows 2 and 4 (light and dark blue, respectively). The cross-correlation coefficient

distribution in Window 1 shows a secondary peak that coincides with the short time delays of Windows 2, 3, and 4. Also, the FR/RSS uncertainty range for Window 1 encompasses lags consistent with 1 day, and the r_{max} is lower compared to temporal Windows 2–5. Despite these anomalous features in the Window 1 CCCD, the peak at ~11 days has a higher maximum cross-correlation coefficient r_{max}, and thus we adopt this as the primary peak during Window 1. Although our chosen windows have sharp boundaries, we have measured the lag in the time intervals both assuming a sudden transition between the intervals as well as a smoother ~10 day transition for each time interval and find that the measured lags are consistent to within 1σ.

As a visual verification of the measured time delays, the right panel of Figure 5 presents the overlapping continuum and "delay-corrected" C IV light curves, which are color coded by the three identified main trends. For illustrative purposes, in each window, the continuum and C IV light curves are normalized to a median of zero and a normalized median absolute deviation (NMAD; e.g., Maronna et al. 2006) of unity. This preserves the shape and variability amplitude of the light curves while enabling a one-to-one comparison between the continuum and the emission-line light-curve features. In general, the normalized and shifted C IV light curves using the individual window lags provide a reasonable match to the features observed in the continuum. The overlapping light curves are also especially instructive for segments of the temporal windows that do not overlap with the continuum features and require careful consideration.

3.4. Variations in the C IV Response

To study the time-dependent variations in the C IV emission-line response to the continuum fluctuations, we follow Goad et al. (2016) in connecting the 1180 Å continuum and C IV reprocessing efficiency η_{eff} using the $F_{C IV} \propto F_{1180}^{\eta_{eff}}$ correlation. We treat the temporal windows identified in Table 2 as independent segments of the light curve and shift back in time each segment of the emission-line light curve by its respective time delay. For the time-delay-corrected continuum flux, we select the continuum flux point closest in time to the shifted emission-line flux. We emphasize that because of the existence of two extended gaps in our observations and the complex light-curve behavior, implementing the weighted approach of Goad et al. (2016) was not feasible for reconstructing the continuum flux. Furthermore, due to the presence of gaps or data associated with the beginning of the campaign, a subset of delay-corrected emission-line fluxes is associated with the same continuum flux measurements, and thus form a cluster of overlapping points in Figure 3. This is more evident in Windows 1 and 5. We include only the first overlapping entry for these clusters of points and exclude the rest from our analysis. We combine all the delay-corrected continuum and emission-line fluxes and obtain the time-averaged emission-line response η_{eff} using the relation

$$\log F_{C\,IV} = A + \eta_{eff} \log F_{1180}, \qquad (3)$$

where A is related to the characteristic EW of C IV at $F_{1180} = 75 \times 10^{-15}$ erg s^{-1} cm^{-2} Å^{-1} as $A = \log[75^{(1-\eta)} \times$ EW$_{C\,IV}$(@75 $\times$ 10^{-15})/100 Å]. We use a linear regression method, including the uncertainties in F_{CIV} and F_{1180}, to determine the C IV marginal response and reprocessing

efficiency as identified by best-fit slope η_{eff} and normalization A. We adopt the `SciKit-learn` linear regression model to perform an ordinary least squares linear regression. We report the best-fit value and 1σ uncertainties using bootstrap sampling of light curves with 1000 realizations with replacement. We report the best-fit η_{eff} and A in Table 3. We combine groups of points with similar C IV flux response at a given continuum flux. We identify three main trends based on the value of the C IV flux at that continuum level, corresponding to Windows 1 and 5, Windows 2 and 4, and Window 3. These relations are shown as best-fit lines in the left panel of Figure 5, with gold corresponding to the high reprocessing efficiency in Window 3 (higher C IV flux at fixed continuum), red showing the lowest reprocessing efficiency in Windows 1 and 5 (lowest C IV flux at fixed continuum), and blue indicates the intermediate reprocessing efficiency in Windows 2 and 4. We also show these three relations as colored lines in Figure 5 and Table 3.

The three lowest F_{1180} flux points in Window 3 seem to influence the slope of the best-fit line. When these three points are removed, the slope is similar to the two lower trends, $\eta_{eff} = 0.31 \pm 0.01$. However, these three points correspond to the three data points immediately before the first safing event, so it is plausible that the delay-corrected emission-line fluxes immediately before the safing gap may not be reliable. This may be because the light curve is already changing but due to overlap with the safing gap it is not captured in the data. The best-fit line to Window 3 with and without the three outlier points is shown in the left panel of Figure 5. The best-fit values are also reported in Table 3. While removing the three points changes the Window 3 slope (dashed yellow line) to be similar to the two lower trends, the intercept remains significantly larger than for the two other trends. This suggests that there may be a difference in the underlying emission-line flux distribution between Window 3 and the other two windows. While it is plausible that the total amount of reprocessing might have changed between the temporal windows since the reprocessing efficiency changes per fixed continuum flux level, the slope similarity suggests that the effective responsivity is approximately the same in each window. This could be caused by a change in the fraction of ionizing photons intercepted by BLR gas (i.e., obscuration) or changes in the spectral shape, in which the extreme-ultraviolet flux has changed relative to the flux of the proxy continuum F_{1180} between one temporal window to the next.

3.5. Obscuration and the C IV Response

A significant element affecting the BLR response in Mrk 817 during STORM 2 is the presence of outflowing gas that obscures the X-ray and ionizing continuum (Paper I). To establish an unobscured baseline, we examine archival spectra of Mrk 817 when it was observed in 2009 using the HST COS instrument (Winter et al. 2011). During these archival observations, the UV spectrum showed no broad absorption troughs (see Figure 2 of Paper I for a comparison between the 2009 archival spectra and those from the AGN STORM 2 campaign). We use the archival spectra to measure the continuum and C IV flux, adopting the continuum windows 1493–1511 Å and 1736–1741.5 Å and an emission-line integration limit of 1590–1638 Å as in Paper II. We find that the unobscured C IV flux response was significantly higher in 2009 (see the gray star symbols in Figure 5). While these C IV
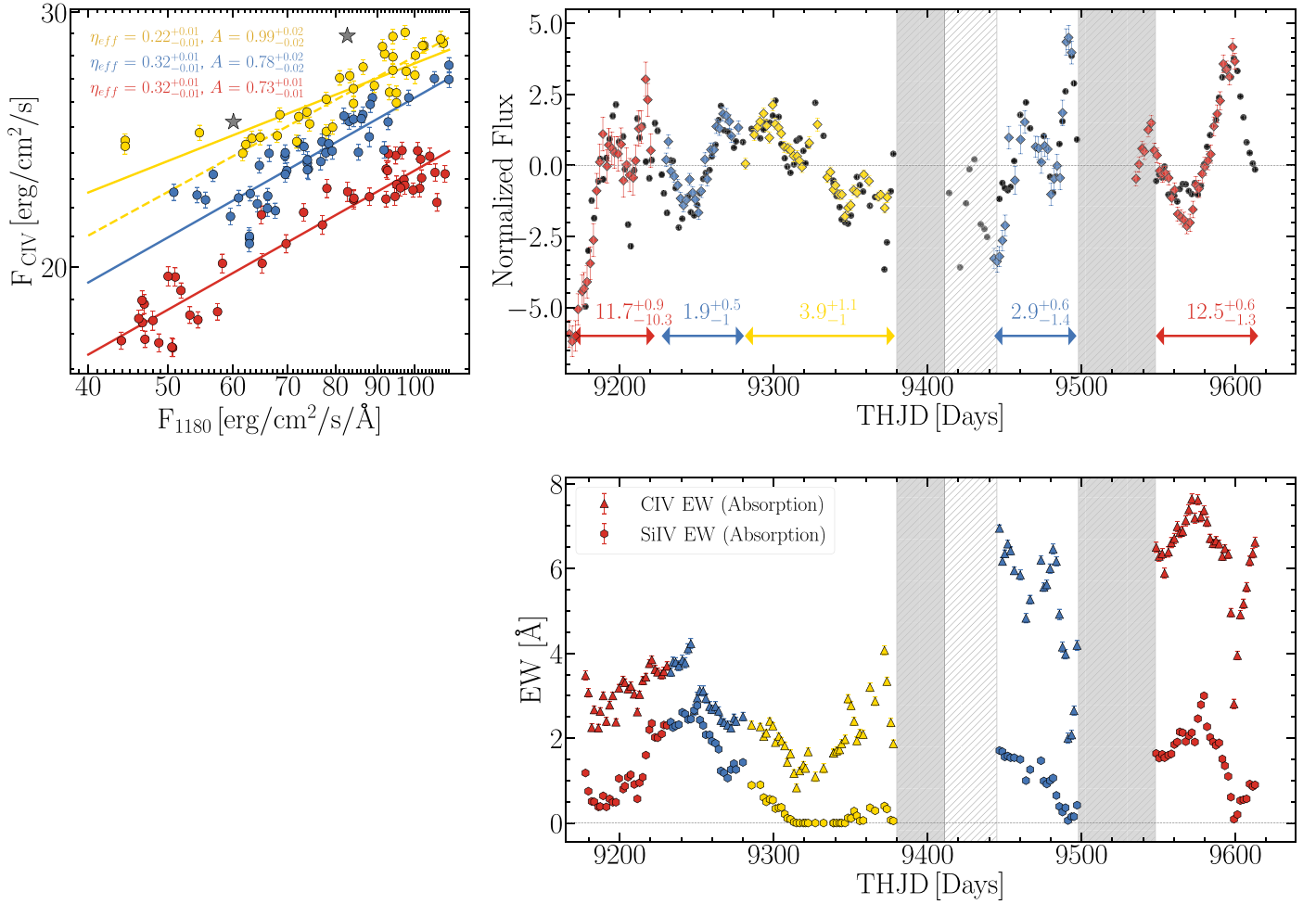
Figure 5. Upper left: Time-delay-corrected fluxes for $F_{C\,IV}$ (in units of 10^{-13} erg s^{-1} cm^{-2} Å^{-1}) vs. the F_{1180} continuum (in units of 10^{-15} erg s^{-1} cm^{-2} Å^{-1}) plotted on a logarithmic scale (similar to Figure 3 but with a different color coding). The color coding represents the three main trends in the C IV emission-line response to continuum variations in Table 3. The best-fit slope to each trend is illustrated with a colored line representing the emission-line responsivity, η_{eff} and A is the best-fit line intercept, as given in the upper left corner (see Equation (3)). The gray stars from archival measurements (uncorrected for time delays) of Mrk 817 obtained in 2009 suggest a significantly higher response and EWs at that time. The yellow dashed line is the fit excluding the three outlier data points in the gold data points. Upper right: The continuum flux F_{1180} (black symbols) overplotted on the $F_{C\,IV}$ light curve (colored symbols) where each light curve is normalized to a median of zero and an NMAD of one and also corrected for the mean time delay in each separate window. Major gaps due to HST safing events are identified by the gray shaded regions. The C IV light curve exhibits a varied behavior in response to the continuum, with the red light-curve segments showing a lag of ~ 11–12.5 days, the blue segments a lag of ~ 2.5 days, and the gold segment a lag of ~ 4 days. Lower right: Time series of the absorption as indicated by Si IV and C IV. Each interval is color coded by the same colors as the light curve. The horizontal line shows the absorption level at zero. The gold symbols correspond to the window where the absorption is at a minimum.

fluxes are higher, and the slope connecting them is steeper than the trends observed in our campaign in the $F_{1180}-F_{C\,IV}$ relation, this cannot be verified since these two isolated archival spectral measurements cannot be placed in context without contemporaneous continuum monitoring to obtain a lag and perform a time-delay correction.

The appearance of the intrinsic UV absorption and blending of the emission lines during the AGN STORM 2 campaign complicates the analysis of the individual spectra. Even though the C IV emission line is the least affected emission line, to investigate a possible phenomenological connection between the intrinsic absorption and the complex C IV response properly, we use a heuristic spectral model to disentangle these complications in the individual spectra. Our spectral modeling is described in Paper I, and it follows the approach adopted by Kaastra et al. (2014) and Kriss et al. (2019) for NGC 5548. We use a reddened power-law continuum plus multiple Gaussian components to fit the emission and broad

absorption features qualitatively. We use multiple Gaussian components to model the emission lines, and we also measure the variable intrinsic broad absorption features, focusing on the strongest ones (P V, C III*, Lyα, N V, Si IV, and C IV). We measure the EW of each absorption line in the normalized spectrum by integrating over pixels lying in the wavelength window of an absorption line. We use this EW as a measure of the strength of the UV absorption and obscuration throughout the campaign. For illustrative purposes, in this paper we focus on the broad Si IV absorption since it is a well-resolved doublet, though we note that all the other broad absorption lines behave similarly. It is important to note here that the absorption EW is measured along our line of sight, but it is not clear how well it tracks the average EW of the absorption present over all lines of sight between the continuum and BLR at a given time.

The C IV line flux in any given window depends on the overall flux from the ionizing continuum that reaches the BLR, and the shape of the transmitted ionizing flux in the spectral
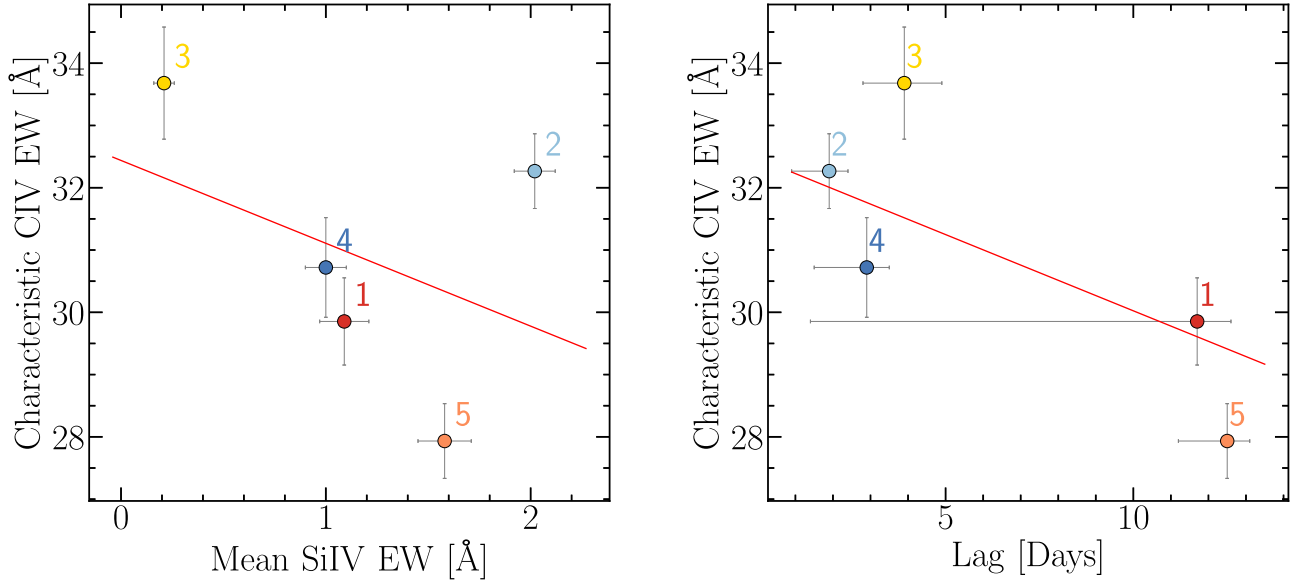
Figure 6. Left: Characteristic C IV EW (as given in Table 3) vs. the mean EW of broad Si IV absorption as a proxy for obscuration in the corresponding time interval. We find a smaller characteristic C IV EW during the temporal windows where the BLR is heavily shielded from the ionizing continuum. Right: Characteristic C IV EW vs. the time lag in the corresponding time interval as given in Table 2. We find longer time delays during the temporal windows where the line response is the lowest (see Figure 8).

Table 3
C IV Response Measurements

Window	THJD (Days)	η_{eff}	A	Characteristic C IV EW (Å)	Best-fit rms
1	9177–9232	$0.16^{+0.02}_{-0.03}$	$1.05^{+0.05}_{-0.05}$	29.9 ± 0.7	2.65%
2	9232–9282	$0.29^{+0.01}_{-0.01}$	$0.84^{+0.03}_{-0.02}$	32.3 ± 0.6	2.55%
3	9282–9378	$0.22^{+0.01}_{-0.01}$	$0.99^{+0.02}_{-0.02}$	33.7 ± 0.9	3.17%
3[a]	9282–9378	$0.31^{+0.01}_{-0.01}$	$0.82^{+0.02}_{-0.02}$	33.6 ± 0.9	3.12%
4	9445–9498	$0.38^{+0.01}_{-0.02}$	$0.65^{+0.03}_{-0.03}$	30.7 ± 0.8	3.26%
5	9548–9615	$0.31^{+0.01}_{-0.01}$	$0.74^{+0.02}_{-0.02}$	27.9 ± 0.6	3.12%
6	9615–9634	$0.06^{+0.04}_{-0.04}$	$1.24^{+0.06}_{-0.06}$	30.0 ± 0.5	1.89 %
1+5	9177–9232 and 9548–9615	$0.32^{+0.01}_{-0.01}$	$0.73^{+0.01}_{-0.01}$	28.5 ± 0.7	3.28%
2+4	9232–9282 and 9445–9498	$0.32^{+0.01}_{-0.01}$	$0.78^{+0.02}_{-0.02}$	32.0 ± 0.8	3.24%

Notes.
[a] We exclude the three data points with the lowest flux in Window 3 and report the fit values. The characteristic C IV EW is the ratio of line flux measured when $F_{1180} = 75 \times 10^{-15}$ erg s^{-1} cm^{-2} Å^{-1} to the continuum $F_{1180} = 75 \times 10^{-15}$ erg s^{-1} cm^{-2} Å^{-1}. We note that the C IV EW was measured using the red wing of the C IV profile due to contamination with absorption. The EW is $\approx 60\%$ of the estimated total flux in C IV, as reported in Paper II.

energy distribution (SED). As one can see from the large scatter in the upper left panel of Figure 5, the observed UV flux F_{1180} appears to be a poor proxy for the ionizing flux, likely due to the strong and variable obscuration. The overall ionizing flux is governed by both the covering factor and column density of the obscurer, while the column density of the obscurer largely governs the shape of the transmitted flux. The characteristic EW as shown in Table 3 and Figure 6 reflects the strength of the reprocessing efficiency for a given time interval and is governed by the total ionizing flux relative to the observed UV continuum. The marginal response of the emission line, η_{eff}, is determined by the shape of the SED in the ionizing UV. In other words, the C IV line flux is a function of the amount of ionizing continuum that reaches the BLR and the shape of the ionizing continuum. The characteristic EW reflects how much of the ionizing continuum is reprocessed into C IV emission while the marginal response reflects how the C IV emission responds to changes in the ionizing continuum.

The bottom right panel in Figure 5 shows the C IV and Si IV absorption light curves. Comparison of the variations in the F_{1180} continuum and C IV emission line with the C IV (top panel of 5) and the Si IV absorption light curves (bottom panel of 5) shows that the temporal windows with the strongest absorption correspond to times when the C IV EW is the smallest (i.e., the reprocessing efficiency is the smallest). Also, but less significantly, weak absorption corresponds to shorter time lags. Figure 6 illustrates these trends more quantitatively. Both panels in Figure 6 show how the normalization of the C IV response function is related to the strength of the broad Si IV absorption (left), and to the measured time lag for that time interval (right). For Si IV the Pearson correlation coefficient $r = -0.43$ with $p = 0.47$, and for the relation versus lag, $r = -0.80$ and $p = 0.10$. Neither trend is statistically significant, primarily due to the large uncertainties, but the qualitative sense one obtains in comparing the light curves is borne out by the trends in the scatter plots, where stronger C IV emission-line

flux and EW correspond to weaker absorption and shorter time lags. This trend is also consistent with the MEMECHO results (Section 3.1). Namely, that the difference in the characteristic EW of C IV as seen in Table 3, the top left panel of Figure 5, and both panels of Figure 6 is generally consistent with the time-dependent background found by MEMECHO, i.e., MEM-ECHO requires a decrease in the relative strength of the C IV line flux, as measured by its characteristic EW, in temporal Windows 1 and 5 (around THJD 9200 and 9600 days). This is in contrast to temporal Window 3, where the C IV flux increases, as measured by the larger characteristic EW.

3.6. Mean and RMS Spectra

To recover any signature of kinematic information about the BLR and thus implications for the light-curve variations, we perform a preliminary comparison of the mean and rms spectra in each of the temporal windows. Similar to Paper II, we isolate the C IV emission line (see Section 4.2 in Paper II). Figure 7 shows the mean and rms spectra for the temporal windows in Table 3. The rms profile, which contains information about the variable part of the spectrum, shows that the most responsive portion of the C IV profile is in the blue side of the profile at negative velocities, and is changing significantly from one temporal window to the next. This may be due to the outflowing wind into our line of sight. Other than the primary peak near the line center at zero velocity that is present in all the temporal windows, Window 2 and Window 4 (light and dark blue, respectively) show the appearance of a secondary peak at a negative velocity. This secondary peak significantly varies in the subsequent temporal windows, and the location of this variation coincides with the broad absorption trough. Also, Window 1 shows the smallest variation amplitude in the rms profile, while Window 2 shows a significantly higher variation amplitude. Initial velocity-binned results from these temporal windows indicate that the signal-to-noise ratio (S/N) is not uniform across all five temporal windows. Consequently, it is challenging to recover information about the dynamics of the C IV emitting region accurately. Therefore, we will defer any 2D RM analysis similar to that of Horne et al. (2021) until we have completed the modeling and corrected for absorption contamination.

4. Discussion

Paper II concluded that the emission-line light curves cannot be explained by a single, static response to the broad UV lines that persists for the duration of the campaign. They are not simply a delayed, proportional response to the continuum variations. Above we showed that by examining individual time segments of the emission-line light curves, we can identify temporal windows where the emission-line gas responds coherently to the continuum variations. Using these temporal windows, we show that the emission-line gas is responding to continuum variations, but the C IV reprocessing efficiency is different from one temporal window to the next. We now discuss possible physical explanations for these variations in emission-line response.

Our hypothesis is that as a consequence of the changes in the ionizing flux illuminating the BLR, due to the evolving properties of the obscuring wind, the region of the BLR responding to the continuum fluctuations changes, leading to changes in the measured time delays. However, the time delays measured in the separate temporal windows behave in a counterintuitive way. During periods of heavy obscuration when the ionizing flux is presumably suppressed, one might expect the time lag to be shorter as the ionization zone producing the maximum C IV flux would be closer to the active nucleus, an effect often described as a "breathing mode" (Gilbert & Peterson 2003; Korista & Goad 2004; Cackett & Horne 2006; Denney et al. 2009; Park et al. 2012; Barth et al. 2015; Runco et al. 2016). In contrast, we find longer lags when the line-of-sight obscuration is stronger, and shorter lags when it is weaker.

The broad extent of the CCF in all the windows (and in all the lines; see the top panel in Figure 4) and from the range in lags from the UV to Hβ (Paper I) shows that the BLR spans radii more than an order of magnitude in size. Describing such a broad distribution with a single number can be misleading since the geometrical distribution of the BLR is convolved with an equally complicated power spectrum of time-variable illuminating radiation. Goad & Korista (2014) studied the consequences of photoionizing a BLR with a large range in radial extent and how it relates to the timescale of the continuum fluctuations. Their simulations show that for rapid continuum fluctuations that occur on timescales shorter than the light-crossing time of the BLR, there is a significant dilution of the observed response of the emission line due to two geometric factors: its finite emissivity volume and its nonnegligible thickness. First, the BLR is not a point source but possesses a characteristic size, often quantified by an emissivity-weighted radius for each emission line. Second, the BLR is not a thin, 2D shell but rather a spatially extended region with an inherent depth. This results in a lower response and longer time delays.

A thought experiment illustrates a plausible scenario that accounts for longer lags being associated with intervals of higher obscuration. The CCF for C IV shows significant response from the BLR over a range of 1–20 lt-days. If we suddenly interpose an opaque screen between the ionizing continuum and the BLR, it is the interior regions of the BLR with the shorter lags that will first notice the lack of continuum radiation and stop responding. More distant regions still "see" the radiation emitted before the screen was in place. The resulting lags we measure, therefore, will be weighted more heavily toward gas at greater distances with longer lags. As this change in obscuration propagates outward and the BLR adjusts to the new level of obscuration, lags will revert to more characteristic, presumably shorter timescales. In addition, the obscuring screen is likely decreasing in opacity, as evidenced by the different tracks in response shown in Figure 5 and by the changing levels of line-of-sight obscuration as measured by the broad UV absorption troughs (bottom panel in Figure 5). This evolution in the line-of-sight obscuration we actually measure from lower values at the beginning of the campaign to a peak ~30 days later may reflect the timescale for gas rising from the accretion disk in the equatorial zone where it obscures the BLR and outflowing to a height where it intercepts the line of sight. For an obscurer located at 1 lt-day near the inner edge of the BLR, the dynamical timescale for a central black hole mass of $3.85 \times 10^7 \, M_\odot$ (Bentz & Katz 2015) is 30 days, consistent with the interpretation that the evolution of the line-of-sight obscuration is due to accretion disk material being lifted off the inner accretion disk and transported on a dynamical timescale to cross our line of sight. Figure 8 illustrates the
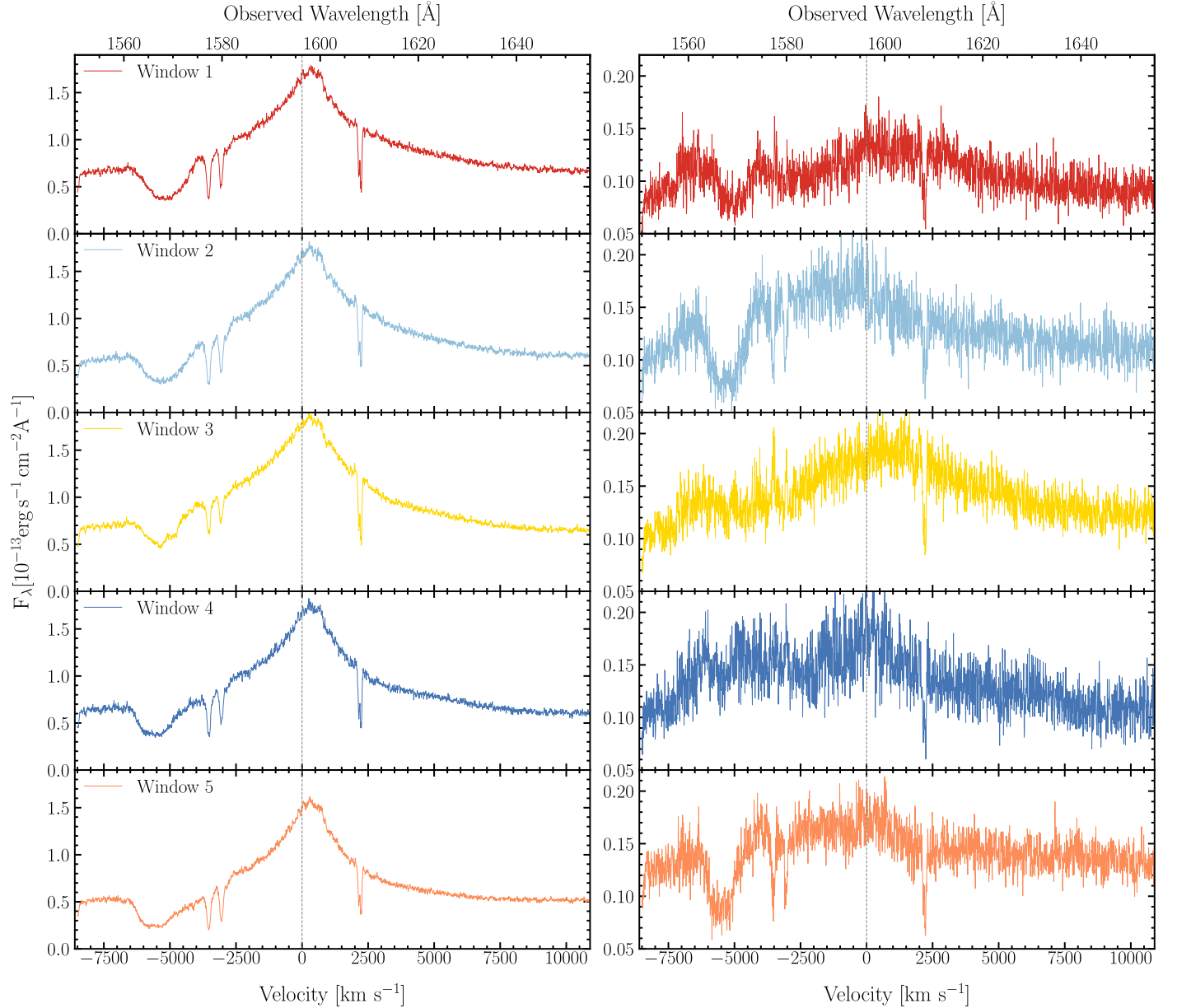
Figure 7. The mean (left) and rms (right) spectra for the temporal windows in Table 3. The rms profile shows significant variations from one temporal window to the next. Other than the primary peak at zero velocity in the rms profile, Window 2 (light blue) shows the appearance of a secondary peak with a negative velocity that significantly varies in the subsequent temporal windows. The location of this variation coincides with the broad absorption trough. Also, Window 1 shows the smallest variation amplitude in the rms profile, while Window 2 shows a significantly higher variation amplitude.

evolution of the obscuration as it blocks the inner BLR from the continuum. We presume that prior to the beginning of the campaign there was no obscuration and the BLR was fully ionized. During Phase A, the obscuration appears and the innermost BLR is shielded first. This causes the shortest lags to disappear. During Phase B, the obscuration flows upwards and outwards into our line of sight over a timescale ~ 30 days, which is the dynamical timescale for material in the inner BLR. At this time, the base of the outflowing wind becomes transparent, and the inner BLR gas can "see" the continuum. In Phase C, the obscuration has lifted and is transparent everywhere, such that the entire BLR is illuminated by the continuum. We also note that as shown by Dehghanian et al. (2020), the energy absorbed by the obscurer is reradiated, but this reemitted radiation is difficult to detect. It is mostly in the form of very broad line emission and diffuse continuum

emission, and its intensity is much reduced since it is isotropically reemitted.

To express these ideas more quantitatively, we follow the arguments by Goad & Korista (2014). AGN variability is well described by a damped random walk (Czerny et al. 2003; Uttley & McHardy 2005; Kelly et al. 2009; Kozłowski et al. 2010; MacLeod et al. 2010; Zu et al. 2011). On short timescales this variability has a power density spectrum that is a power law with a spectral index of -2. To understand the BLR response in Mrk 817, the essential feature is that short-timescale continuum fluctuations have less power and lower amplitude than those at longer timescales. When the ionizing continuum is heavily obscured, the amplitude of continuum fluctuations as seen by the BLR is significantly reduced. Although amplitudes are suppressed on all timescales by the

Figure 8. Schematic view of the BLR. The STORM 2 campaign observed three phases of obscuration and outflow. The top panel shows these three main phases. In each phase, the BLR gas is illustrated by clouds. Those BLR clouds unobscured by the partially opaque, outflowing gas are shown in green. By contrast, those clouds that lie within the shadow of the obscuration are illustrated as uncolored. The thick arrow shows the obscuration, the ionizing continuum emission is identified by the collection of purple arrows, and the ever-present outflow is shown as a stream that is launched from the accretion disk. In Phase A, obscuration blocks the inner BLR from the continuum emission. Shorter lags disappear because it takes longer for the BLR gas at larger radii to realize that the continuum emission is blocked (Windows 1 and 5). During Phase B, the obscuration flows upwards and outwards into our line of sight. The base of the wind becomes transparent so that the continuum emission once again reaches the inner edge of the BLR. During this time we "see" short lags since only the inner BLR region reprocesses the continuum emission (Windows 2 and 4). Then, in Phase C, the obscuration at low elevations becomes transparent enough for the continuum emission to reach all of the BLR clouds uniformly, presumably the true extent of the BLR. The bottom panel shows the C IV light curve, and the five identified windows. The colored frames on each window of the light curve correspond to the matched-color phase. Phase A corresponds to Windows 1 and 5, Phase B corresponds to Windows 2 and 4, and Window 3 corresponds to Phase C. The gray shadings, which illustrate the two HST safing incidents, could plausibly undergo a similar scenario. Although our schematic is 2D, we argue that the variations in the emission line require the obscuration to be azimuthally symmetric, as the observed changes in response encompass the entire BLR, not just our line of sight.

obscuration, the S/N we achieve in our observations limits our ability to detect some amplitudes and timescales.

The low-amplitude, short-timescale, rapid fluctuations that we see in the observable UV are suppressed in the ionizing continuum viewed by the BLR, up to as much as a factor of 10 for the 90% covering fractions seen in the X-ray (Partington et al. 2023). This prediction of a reduced amplitude of fluctuations in the BLR is consistent with the significantly lower amplitudes in the rms spectrum for Window 1 as seen in the top right-hand panel of Figure 7. So, even though our flux measurement errors of better than 1.5% allow us to see easily a response to 5%–10% fluctuations when the source is unobscured, these become undetectable during periods of heavy obscuration. During these periods we are only able to measure a response in the BLR for the stronger variations (50% to 200%) on longer timescales. Following the simulations of Goad et al. (2004), this favors recovering a CCF with longer lags. However, note that a short-timescale response is still present in the CCFs for temporal Windows 1–5 (see the second panel in Figure 4) even though it is not dominant. In particular, notice the secondary peak for Window 1 at the short lags typical of the lightly obscured Window 3. During the more transparent phase, Window 3, the BLR is illuminated by the full ionizing continuum, with all the rapid fluctuations we see in the observable UV also present in the variations of the

ionizing flux. These more rapid variations are diminished at large radii by geometrical dilution, so the CCF is biased toward shorter timescales, and the peak shifts to short lags.

A similar process with the appearance of the injection of a new screen of opaque material into the outflow may have occurred at the end of the campaign (Window 6), which may be indicative of a nonresponsive "holiday" interval in the C IV flux during the last nine epochs of the HST campaign. This might be testable with the behavior of the Hβ emission line as tracked by the ongoing ground-based campaign.

5. Summary and Future Work

The AGN STORM 2 campaign of Mrk 817 reveals complexities in BLR structure and its response to continuum fluctuations that go beyond the simplest concepts originally envisioned for RM experiments. As noted in Paper II, the emission-line light curves for Mrk 817 are not merely smoothed, shifted, and scaled versions of the continuum light curve. In this paper we have shown that different temporal windows in the STORM 2 campaign have different responses to the continuum fluctuations, with the C IV emission-line flux in each time interval showing a different response to continuum fluctuations, and a different time lag. These time lags range from 2 to 13 days. The different temporal windows correspond

to significant variations in the properties of the obscuring gas. Temporal windows with the longest lags correspond to periods of increasing obscuration, with the obscurer shielding and diminishing the response of the innermost regions of the BLR. The temporal windows with the shortest lags occur in intervals with diminishing obscuration. The changing SED of the ionizing flux reaching the BLR may be responsible for the changes in the line responses in the different temporal windows.

In future work, once we have modeled the effects of absorption on the emission-line profiles and deblended the adjacent emission lines, we will extend the analysis presented here to Lyα, N V, Si IV, and He II.

Appendix
Considerations for Temporal Window Selections

To test for possible time interval edge effects, given the anticipated C IV time delays, we extend the length of each time interval. We modify the start date of the F_{1180} continuum points to start 10 days earlier and also extend the end dates of the C IV light curves to be 10 days later than the dates reported in Table 1. The reported lag measurements in Table 2 are the result of this extended continuum search range. We find that these extended boundaries result in time delays that are consistent within 1σ with the exact time interval ranges reported in Table 1.

We also note that the data immediately after the first HST safing event are more sparsely sampled for ∼30 days and have a longer mean cadence of 4 days (compared to the expected 2 day cadence). This raises two issues. First, since the continuum light curve is driving the emission-line response, the absence of continuum data during the safing event makes it difficult to measure a response for observations immediately following the safing interval. Second, the larger intervals between the observations immediately after the safing event degrade the resolution of the time-delay measurement. Therefore, we exclude THJD = 9413–9445 from this window, ensuring sufficient sampling and giving some continuum coverage postsafing. Thus we only consider THJD = 9445–9498 for Window 4 (blue). We do not face the same issue following the second safing event, since the light-curve sampling is uniform right after the safing incident and consistent with the expected 2 day cadence.

Near the end of the campaign, after the last continuum peak at THJD ≈ 9600 (see Figure 1), the BLR response to the diminishing continuum is significantly reduced, where the continuum falls by a factor of 2 in 20 days, but the line fluxes fall by only a few percent. Although the continuum flux is rising after THJD = 9615, only Lyα shows a clear response. All other emission lines, including C IV, remain less responsive, suggesting that the BLR may have entered another holiday period at the end of the campaign. This decorrelation continues for the remaining 20 days of the campaign. We therefore end Window 5 at THJD = 9615 (orange), and we do not carry out a detailed time-delay analysis of Window 6 (light blue).

In summary, the periods that we remove from the time-delay measurements are:

1. THJD = 9413–9445, due to sparse sampling (mean of 4 days) immediately after an extended HST safing gap.
2. THJD = 9615–9634, due to the likelihood of entering a BLR holiday state (Goad et al. 2016).

ORCID iDs

Y. Homayouni ⓘ https://orcid.org/0000-0002-0957-7151
Gerard A. Kriss ⓘ https://orcid.org/0000-0002-2180-8266
Gisella De Rosa ⓘ https://orcid.org/0000-0003-3242-7052
Rachel Plesha ⓘ https://orcid.org/0000-0002-2509-3878
Edward M. Cackett ⓘ https://orcid.org/0000-0002-8294-9281
Michael R. Goad ⓘ https://orcid.org/0000-0002-2908-7360
Kirk T. Korista ⓘ https://orcid.org/0000-0003-0944-1008
Keith Horne ⓘ https://orcid.org/0000-0003-1728-0304
Travis Fischer ⓘ https://orcid.org/0000-0002-3365-8875
Tim Waters ⓘ https://orcid.org/0000-0002-5205-9472
Aaron J. Barth ⓘ https://orcid.org/0000-0002-3026-0562
Erin A. Kara ⓘ https://orcid.org/0000-0003-0172-0854
Hermine Landt ⓘ https://orcid.org/0000-0001-8391-6900
Nahum Arav ⓘ https://orcid.org/0000-0003-2991-4618
Benjamin D. Boizelle ⓘ https://orcid.org/0000-0001-6301-570X
Misty C. Bentz ⓘ https://orcid.org/0000-0002-2816-5398
Michael S. Brotherton ⓘ https://orcid.org/0000-0002-1207-0909
Doron Chelouche ⓘ https://orcid.org/0000-0002-4830-7787
Elena Dalla Bontà ⓘ https://orcid.org/0000-0001-9931-8681
Maryam Dehghanian ⓘ https://orcid.org/0000-0002-0964-7500
Pu Du ⓘ https://orcid.org/0000-0002-5830-3544
Gary J. Ferland ⓘ https://orcid.org/0000-0003-4503-6333
Carina Fian ⓘ https://orcid.org/0000-0002-2306-9372
Jonathan Gelbord ⓘ https://orcid.org/0000-0001-9092-8619
Catherine J. Grier ⓘ https://orcid.org/0000-0001-9920-6057
Patrick B. Hall ⓘ https://orcid.org/0000-0002-1763-5825
Dragana Ilić ⓘ https://orcid.org/0000-0002-1134-4015
Michael D. Joner ⓘ https://orcid.org/0000-0003-0634-8449
Jelle Kaastra ⓘ https://orcid.org/0000-0001-5540-2822
Shai Kaspi ⓘ https://orcid.org/0000-0002-9925-534X
Andjelka B. Kovačević ⓘ https://orcid.org/0000-0001-5139-1978
Daniel Kynoch ⓘ https://orcid.org/0000-0001-8638-3687
Yan-Rong Li ⓘ https://orcid.org/0000-0001-5841-9179
Missagh Mehdipour ⓘ https://orcid.org/0000-0002-4992-4664
Jake A. Miller ⓘ https://orcid.org/0000-0001-8475-8027
John Montano ⓘ https://orcid.org/0000-0001-5639-5484
Hagai Netzer ⓘ https://orcid.org/0000-0002-6766-0260
J. M. M. Neustadt ⓘ https://orcid.org/0000-0001-7351-2531
Ethan Partington ⓘ https://orcid.org/0000-0003-1183-1574
Luka Č. Popović ⓘ https://orcid.org/0000-0003-2398-7664
Daniel Proga ⓘ https://orcid.org/0000-0002-6336-5125
Thaisa Storchi-Bergmann ⓘ https://orcid.org/0000-0003-1772-0023
David Sanmartim ⓘ https://orcid.org/0000-0002-9238-9521
Matthew R. Siebert ⓘ https://orcid.org/0000-0003-2445-3891
Tommaso Treu ⓘ https://orcid.org/0000-0002-8460-0390
Marianne Vestergaard ⓘ https://orcid.org/0000-0001-9191-9837
Jian-Min Wang ⓘ https://orcid.org/0000-0001-9449-9268
Martin J. Ward ⓘ https://orcid.org/0000-0003-1810-0889
Fatima Zaidouni ⓘ https://orcid.org/0000-0003-0931-0868
Ying Zu ⓘ https://orcid.org/0000-0001-6966-6925

References

Alexander, T. 1997, in Astronomical Time Series, ed. D. Maoz, A. Sternberg, & E. M. Leibowitz, Vol. 218 (Dordrecht: Kluwer)
Alexander, T. 2013, arXiv:1302.1508

Bahcall, J. N., Kozlovsky, B.-Z., & Salpeter, E. E. 1972, ApJ, 171, 467
Baldwin, J. A. 1977, ApJ, 214, 679
Bao, D.-W., Brotherton, M. S., Du, P., et al. 2022, ApJS, 262, 14
Barth, A. J., Bennert, V. N., Canalizo, G., et al. 2015, ApJS, 217, 26
Barth, A. J., Nguyen, M. L., Malkan, M. A., et al. 2011, ApJ, 732, 121
Bentz, M. C., Denney, K. D., Grier, C. J., et al. 2013, ApJ, 767, 149
Bentz, M. C., & Katz, S. 2015, PASP, 127, 67
Bentz, M. C., Walsh, J. L., Barth, A. J., et al. 2009, ApJ, 705, 199
Bentz, M. C., Walsh, J. L., Barth, A. J., et al. 2010, ApJ, 716, 993
Bentz, M. C., Williams, P. R., Street, R., et al. 2021, ApJ, 920, 112
Blandford, R. D., & McKee, C. F. 1982, ApJ, 255, 419
Brotherton, M. S., Du, P., Xiao, M., et al. 2020, ApJ, 905, 77
Cackett, E. M., Bentz, M. C., & Kara, E. 2021, iScience, 24, 102557
Cackett, E. M., Gelbord, J., Barth, A. J., et al. 2023, ApJ, 958, 195
Cackett, E. M., & Horne, K. 2006, MNRAS, 365, 1180
Clavel, J., Reichert, G. A., Alloin, D., et al. 1991, ApJ, 366, 64
Czerny, B., Doroshenko, V. T., Nikołajuk, M., et al. 2003, MNRAS, 342, 1222
De Rosa, G., Fausnaugh, M. M., Grier, C. J., et al. 2018, ApJ, 866, 133
De Rosa, G., Peterson, B. M., Ely, J., et al. 2015, ApJ, 806, 128
Dehghanian, M., Ferland, G. J., Kriss, G. A., et al. 2019, ApJ, 877, 119
Dehghanian, M., Ferland, G. J., Kriss, G. A., et al. 2020, ApJ, 898, 141
Denney, K. D., Peterson, B. M., Pogge, R. W., et al. 2009, ApJL, 704, L80
Denney, K. D., Peterson, B. M., Pogge, R. W., et al. 2010, ApJ, 721, 715
Du, P., Brotherton, M. S., Wang, K., et al. 2018, ApJ, 869, 142
Du, P., Lu, K.-X., Hu, C., et al. 2016, ApJ, 820, 27
Ebrero, J., Kriss, G. A., Kaastra, J. S., & Ely, J. C. 2016, A&A, 586, A72
Edelson, R., Gelbord, J. M., Horne, K., et al. 2015, ApJ, 806, 129
Fausnaugh, M. M., Denney, K. D., Barth, A. J., et al. 2016, ApJ, 821, 56
Gaskell, C. M., & Peterson, B. M. 1987, ApJS, 65, 1
Gaskell, C. M., & Sparke, L. S. 1986, ApJ, 305, 175
Gilbert, K. M., & Peterson, B. M. 2003, ApJ, 587, 123
Goad, M. R., & Korista, K. T. 2014, MNRAS, 444, 43
Goad, M. R., & Korista, K. T. 2015, MNRAS, 453, 3662
Goad, M. R., Korista, K. T., De Rosa, G., et al. 2016, ApJ, 824, 11
Goad, M. R., Korista, K. T., & Knigge, C. 2004, MNRAS, 352, 277
Green, J. C., Froning, C. S., Osterman, S., et al. 2012, ApJ, 744, 60
Grier, C. J., Peterson, B. M., Horne, K., et al. 2013, ApJ, 764, 47
Homayouni, Y., De Rosa, G., Plesha, R., et al. 2023, ApJ, 948, 85
Horne, K. 1994, in ASP Conf. Ser. 69, Reverberation Mapping of the Broad-Line Region in Active Galactic Nuclei, ed. P. M. Gondhalekar, K. Horne, & B. M. Peterson (San Francisco, CA: ASP), 23
Horne, K., De Rosa, G., Peterson, B. M., et al. 2021, ApJ, 907, 76
Horne, K., Peterson, B. M., Collier, S. J., & Netzer, H. 2004, PASP, 116, 465
Horne, K., Welsh, W. F., & Peterson, B. M. 1991, ApJL, 367, L5
Kaastra, J. S., Kriss, G. A., Cappi, M., et al. 2014, Sci, 345, 64
Kara, E., Mehdipour, M., Kriss, G. A., et al. 2021, ApJ, 922, 151
Kaspi, S., Smith, P. S., Netzer, H., et al. 2000, ApJ, 533, 631
Kelly, B. C., Bechtold, J., & Siemiginowska, A. 2009, ApJ, 698, 895
Kinney, A. L., Rivolo, A. R., & Koratkar, A. P. 1990, ApJ, 357, 338
Korista, K. T., & Goad, M. R. 2004, ApJ, 606, 749
Kovačević, A., Popović, L. Č, Shapovalova, A. I., & Ilić, D. 2017, Ap&SS, 362, 31
Kozłowski, S., Kochanek, C. S., Udalski, A., et al. 2010, ApJ, 708, 927
Kriss, G. A., De Rosa, G., Ely, J., et al. 2019, ApJ, 881, 153
Krolik, J. H., Horne, K., Kallman, T. R., et al. 1991, ApJ, 371, 541
Krolik, J. H. 1999, Active Galactic Nuclei. From the Central Black Hole to the Galactic Environment (Princeton, NJ: Princeton Univ. Press)
Li, Y.-R., Songsheng, Y.-Y., Qiu, J., et al. 2018, ApJ, 869, 137
Lira, P., Kaspi, S., Netzer, H., et al. 2018, ApJ, 865, 56
Longinotti, A. L., Kriss, G., Krongold, Y., et al. 2019, ApJ, 875, 150
Longinotti, A. L., Krongold, Y., Kriss, G. A., et al. 2013, ApJ, 766, 104
MacLeod, C. L., Ivezić, Ž., Kochanek, C. S., et al. 2010, ApJ, 721, 1014
Maronna, R. A., Martin, R. D., & Yohai, V. J. 2006, Robust Statistics (New York: Wiley)
Mathur, S., Gupta, A., Page, K., et al. 2017, ApJ, 846, 55
Mehdipour, M., Kaastra, J. S., Kriss, G. A., et al. 2017, A&A, 607, A28
Miller, J. M., Zoghbi, A., Reynolds, M. T., et al. 2021, ApJL, 911, L12
Osmer, P. S., Porter, A. C., & Green, R. F. 1994, ApJ, 436, 678
Pancoast, A., Brewer, B. J., & Treu, T. 2011, ApJ, 730, 139
Pancoast, A., Brewer, B. J., Treu, T., et al. 2014, MNRAS, 445, 3073
Park, D., Kelly, B. C., Woo, J.-H., & Treu, T. 2012, ApJS, 203, 6
Parker, M. L., Longinotti, A. L., Schartel, N., et al. 2019, MNRAS, 490, 683
Partington, E. R., Cackett, E. M., Kara, E., et al. 2023, ApJ, 947, 2
Pedregosa, F., Varoquaux, G., Gramfort, A., et al. 2011, JMLR, 12, 2825
Pei, L., Fausnaugh, M. M., Barth, A. J., et al. 2017, ApJ, 837, 131

Peterson, B. M. 1993, PASP, 105, 247

Peterson, B. M., Balonek, T. J., Barker, E. S., et al. 1991, ApJ, 368, 119

Peterson, B. M., De Rosa, G., Kriss, G. A., et al. 2020, HST Proposal 16196

Peterson, B. M., Ferrarese, L., Gilbert, K. M., et al. 2004, ApJ, 613, 682

Peterson, B. M., Wanders, I., Bertram, R., et al. 1998, ApJ, 501, 82

Plesha, R., Kriss, G., de Rosa, G., & Homayouni, Y. 2023, Data from Space Telescope and Optical Reverberation Mapping of Mrk 817 (STORM2), STScI/MAST, doi:10.17909/N734-K698

Pogge, R. W., & Peterson, B. M. 1992, AJ, 103, 1084

Runco, J. N., Cosens, M., Bennert, V. N., et al. 2016, ApJ, 821, 33

Sun, M., Grier, C. J., & Peterson, B. M., 2018 PyCCF: Python Cross Correlation Function for Reverberation Mapping Studies, Astrophysics Source Code Library, ascl:1805.032

U, V., Barth, A. J., Vogler, H. A., et al. 2022, ApJ, 925, 52

Ulrich, M.-H., & Horne, K. 1996, MNRAS, 283, 748

Uttley, P., & McHardy, I. M. 2005, MNRAS, 363, 586

Villafaña, L., Williams, P. R., Treu, T., et al. 2022, ApJ, 930, 52

Wang, Y., Kaastra, J., Mehdipour, M., et al. 2022, A&A, 657, A77

Welsh, W. F., & Horne, K. 1991, ApJ, 379, 586

White, R. J., & Peterson, B. M. 1994, PASP, 106, 879

Winter, L. M., Danforth, C., Vasudevan, R., et al. 2011, ApJ, 728, 28

Zu, Y., Kochanek, C. S., & Peterson, B. M. 2011, ApJ, 735, 80